

How Doped MoS₂ Breaks Transition-Metal Scaling Relations for CO₂ Electrochemical Reduction

Xin Hong,^{†,§} Karen Chan,^{†,§} Charlie Tsai,[†] and Jens K. Nørskov^{*,†,‡}

[†]SUNCAT Center for Interface Science and Catalysis, Department of Chemical Engineering, Stanford University, Stanford, California 94305, United States

[‡]SUNCAT Center for Interface Science and Catalysis, SLAC National Accelerator Laboratory, 2575 Sand Hill Road, Menlo Park, California 94025, United States

S Supporting Information

ABSTRACT: Linear scaling relationships between the adsorption energies of CO₂ reduction intermediates pose a fundamental limitation to the catalytic efficiency of transition-metal catalysts. Significant improvements in CO₂ reduction activity beyond transition metals require the stabilization of key intermediates, COOH* and CHO* or COH*, independent of CO*. Using density functional theory (DFT) calculations, we show that the doped sulfur edge of MoS₂ satisfies this requirement by binding CO* significantly weaker than COOH*, CHO*, and COH*, relative to transition-metal surfaces. The structural basis for the scaling of doped sulfur edge of MoS₂ is due to CO* binding on the metallic site (doping metal) and COOH*, CHO*, and COH* on the covalent site (sulfur). Linear scaling relations still exist if all the intermediates bind to the same site, but the combined effect of the two binding sites results in an overall deviation from transition-metal scaling lines. This principle can be applied to other metal/*p*-block materials. We rationalize the weak binding of CO* on the sulfur site with distortion/interaction and charge density difference analyses.

KEYWORDS: electrocatalysis, CO₂ reduction, density functional theory, scaling relationship, MoS₂



INTRODUCTION

Electroreduction of CO₂ in an efficient and selective manner under ambient conditions would allow for the storage of energy in carbon-based products from a range of renewable energy resources.¹ Currently, significant improvements for the catalytic efficiency and selectivity are required to achieve a viable transformation.² Copper, the only transition-metal catalyst that produces hydrocarbons at high Faradaic efficiency, requires an overpotential of ~1 V to produce a current density of 1 mA/cm².³ Gold catalysts are selective for CO production, but still require an overpotential of more than 0.3 V with a current density of 0.2 mA/cm² at pH 7.⁴

Previous computational studies of CO₂ reduction on transition-metal surfaces have illustrated the linear scaling relationship between the adsorption energies of the key CO₂ reduction intermediates, COOH*, CO*, and CHO*.⁵ These relations suggest that the key reduction intermediates, COOH* and CHO*, cannot be stabilized independently of CO*.⁵ Such a stabilization is a necessary, but not sufficient condition for a low overpotential catalyst. The existence of activation barriers can impose additional constraints. However, the existence of these scaling relations is consistent with the persistent overpotential observed in experiments and poses a fundamental limitation to the catalytic efficiency of transition-metal catalysts for CO₂ electroreduction.⁶

Our recent study has demonstrated that the active edge sites of MoS₂ and MoSe₂ do not follow linear scaling between

COOH*/CHO* and CO*.⁷ These materials bind COOH* and CHO* significantly stronger than CO*, which opens the possibility for an improvement of the CO₂ reduction activity, in comparison to transition-metal surfaces.^{7c} In addition, experiments have shown that MoS₂, in the presence of an imidazolium ionic liquid, has superior CO₂ reduction activity, relative to nanostructured transition-metal catalysts.⁸

In this work, we use density functional theory (DFT) calculations to investigate the scaling relations for various doped MoS₂. The dopant metal provides an additional dimension to tune the scaling to design better catalysts. We found the dual binding sites in these materials to be the structural basis for breaking linear scaling, and the competition between the two binding sites is studied through a distortion/interaction model and electron density analysis.

Computational Details. MoS₂ has a single layered, S–Mo–S sandwich structure. Mo atoms are arranged in a hexagonal lattice and in trigonal prismatic coordination with two S layers. There are two types of edges in MoS₂: an (1010) edge, known as the sulfur edge, and an (1010) edge, known as the molybdenum edge.^{7c,9} We have focused on the doping of sulfur edge of MoS₂, and a schematic of Ni-doped MoS₂ is shown in Figure 1. Experiments have shown that Fe-, Co-, Ni-,

Received: February 29, 2016

Revised: May 12, 2016

Published: May 27, 2016

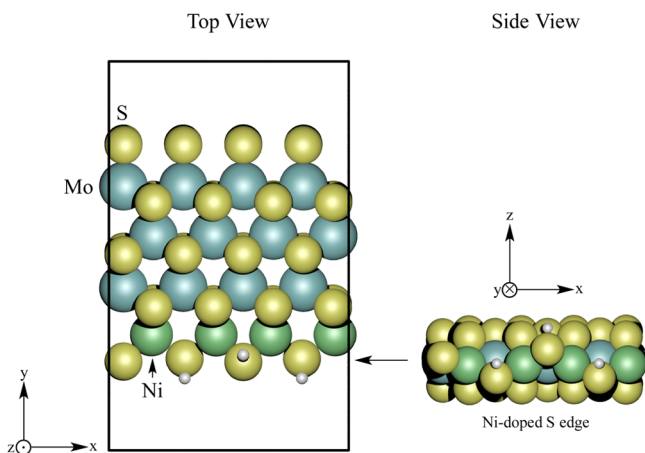


Figure 1. Doped sulfur edge in the stripe model of Ni-doped MoS₂. The box shows the periodic unit cell used in the calculations.

and Cu-doped MoS₂ preferentially have the Mo atom at the sulfur edge substituted¹⁰ and theoretical studies on doped MoS₂ clusters have showed that the sulfur edge is usually less stable and more prone to doping.¹¹

The layered MoS₂ structures have an extra level of complexity regarding the coverage of H and S under the reaction conditions. We have determined the most stable structures for each doped MoS₂, and the most stable coverage has $\theta_s = 0.5$ in most cases, which are labeled with the doping metal in the following figures. With certain dopants, two coverages ($\theta_s = 0.5$ and $\theta_s = 0.75$) are similar in stability, in which case both are considered. The label “Metal(1)” refers to the doped MoS₂ with $\theta_s = 0.5$, and “Metal(2)” refers to the doped MoS₂ with $\theta_s = 0.75$. Further details on coverage determination are discussed in the [Supporting Information](#).

DFT calculations were performed with the QUANTUM ESPRESSO code¹² and the BEEF-vdW exchange-correlation functional,¹³ which was applied in a plane-wave ultrasoft pseudopotential implementation. Plane-wave and density cutoffs were 500 and 5000 eV, respectively, with a Fermi-level smearing width of 0.1 eV and $(2 \times 2 \times 1)$ *k*-point sampling, based on convergence tests from previous work.^{7d} For Fe-doped MoS₂, the plane-wave and density cutoffs were 800 and 8000 eV, respectively. The calculated lattice constant for MoS₂ was $a = 3.21$ Å, in agreement with experimental results ($a = 3.16$ Å).¹⁴ We used a unit cell to include four Mo atoms wide in the *x*- and *y*-directions, with a single layer of MoS₂. Periodic boundary conditions were applied and 11 and 9 Å of vacuum were used on the planes and edges, respectively. All structures were relaxed until all force components were <0.05 eV Å⁻¹. Spin-polarized calculations were performed for the Cr-, Co-, Fe-, Mn-, and Ni-doped cases. Further calculation details are given in the [Supporting Information](#).

Binding energies of all reaction intermediates were constructed using the computational hydrogen electrode (CHE) model.¹⁵ This model provides a simple and straightforward approach to account for the influence of potential on the free-energy changes, without the explicit consideration of solvent, applied potential, or solvated protons, which are very challenging to treat atomistically.¹⁶ Further details regarding the use of CHE are included in the [Supporting Information](#).

RESULTS AND DISCUSSION

Binding Energies of *COOH, *CO, *CHO, and *COH on Doped MoS₂. Generally, the initial reduction steps of CO₂ have the highest limiting potentials, so the binding energies of COOH*, CO*, and CHO* determine the limiting potential and the overall reaction rate.^{6,7c} On transition-metal surfaces, the intermediates bind through the same site, and a linear scaling relationship exists among binding energies. This scaling severely limits the minimum achievable overpotential in CO₂ reduction.¹⁷ As shown in [Figures 2](#) and [3](#), the scaling

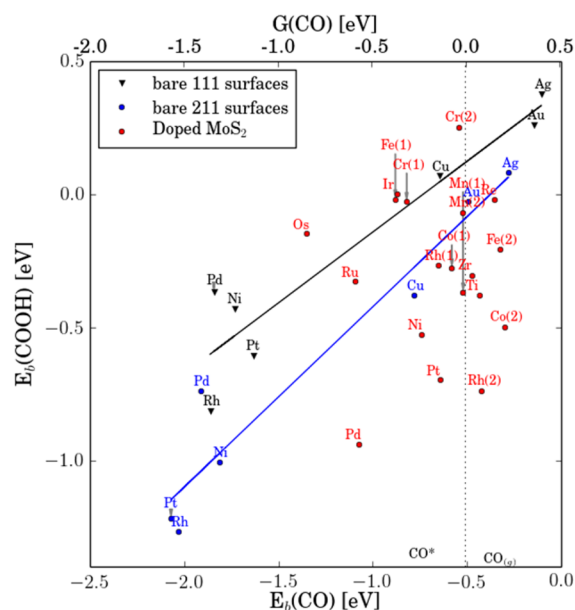


Figure 2. Binding energies $E_b(\text{COOH})$ vs $E_b(\text{CO})$ for the doped sulfur edge of MoS₂, as well as the transition-metal (111) and (211) scaling relations. The vertical dotted lines indicate the $E_b(\text{CO})$ value at which an isolated CO* is in equilibrium with 0.01 bar of gaseous CO. The catalysts to the right of this line bind CO weakly and are expected to be selective for CO production; the catalysts to the left should further reduce adsorbed CO to hydrocarbons and/or alcohols.

relationships on transition-metal (111) and (211) surfaces suggest that one cannot stabilize COOH* or CHO*, independent of CO*. Assuming CO* to CHO* to be the limiting step for CO₂ reduction to hydrocarbons, the limiting potential is overlaid in [Figure 3](#). This figure shows the dramatic reduction in limiting potential that can be achieved with catalysts that break transition-metal scaling by stabilizing CHO* more than CO*.

While the limiting potential is only a thermodynamic measure and does not necessarily reflect the kinetic barrier, our previous studies have shown that the limiting potential to be consistent with the trends in activity for CO₂ reduction on transition metals,⁵ as well as the onset potential for the formation of CO₂ reduction products on Cu.¹⁸ We attribute this agreement to the scaling between activation and reaction energies for surface reactions.¹⁹ Trends in H₂ evolution activity are also consistent with the limiting potential of H₂ on both transition metals and MoS₂.^{9a,20} Therefore, catalysts with low limiting potentials relative to existing transition-metal catalysts should have the possibility of a higher CO₂ reduction activity.

As shown in [Figures 2](#) and [3](#), doped MoS₂ do not follow the linear scaling relationship of pure metal surfaces, and the scatter allows some of the doped MoS₂ to approach the desired region

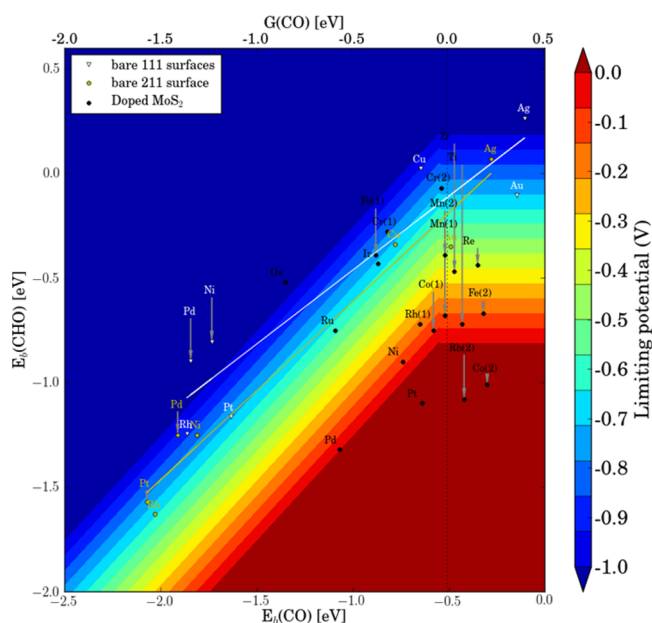


Figure 3. Binding energies $E_b(\text{CHO})$ vs $E_b(\text{CO})$ for the doped sulfur edge of MoS_2 , as well as the transition-metal (111) and (211) scaling relations. The colorful contour plot represents the limiting potential of the CO^* -to- CHO^* step.

of high efficiency for CO_2 reduction. Among the various dopants, Ni is the most promising candidate, in terms of scaling and low cost.

In addition, we have examined the scaling relationships between COH^* and CO^* on transition-metal surfaces and doped MoS_2 , and the results are shown in Figure 4. Similar to CHO^* , COH^* also does not scale linearly with CO^* . COH^* generally binds the surface through the bridging site between

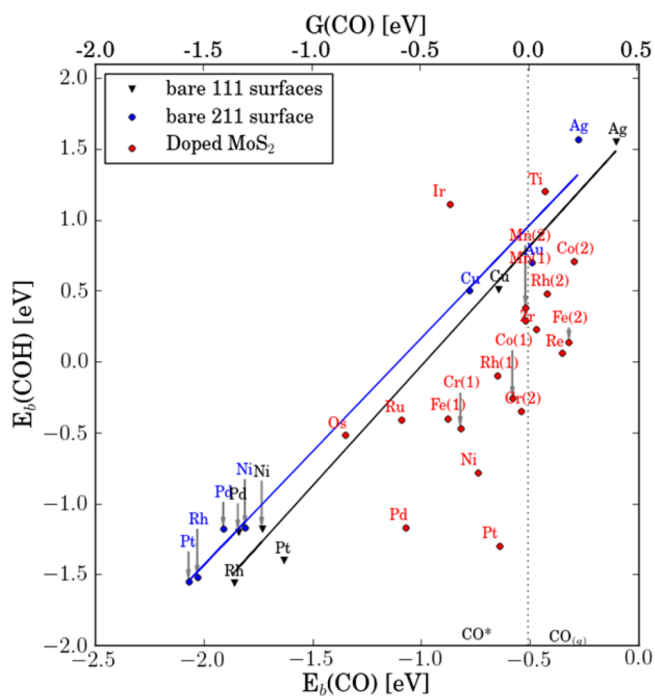


Figure 4. Binding energies $E_b(\text{COH})$ vs $E_b(\text{CO})$ for the doped sulfur edge of MoS_2 , as well as the transition-metal (111) and (211) scaling relations.

the doping metal and sulfur. Similar to that observed in transition metals, COH^* is generally much less stable than CHO^* for various doped MoS_2 and does not play an important role in determining the CO_2 reduction kinetics for these dopants (Figure 5).

Free-Energy Surfaces of CO_2 Reduction with Ni- and Co-doped MoS_2 . To confirm that the optimal binding of the CO , CHO , and/or COOH reduction intermediates leads to improved catalytic performance, we also studied the free-energy changes of the entire CO_2 reduction catalytic cycles with two of the best nonprecious metal dopants, nickel and cobalt. Figure 6 shows the free-energy surface for CO_2 reduction on the Ni-doped sulfur edge of MoS_2 . Because the nickel dopant breaks the CO – CHO scaling significantly, this step is only uphill by 0.12 eV. With this catalyst, the potential-limiting step is CHO to formaldehyde, and the overpotential of the entire catalytic cycle is only 0.28 eV, which is much lower than those of pure transition-metal surfaces. As shown in Figure 7, the cobalt dopant also has a facile CO -to- CHO step. This again changes the potential-limiting step, and the CO_2 -to- COOH step limits the overall efficiency of the entire catalytic cycle. The overpotential with the Co dopant is 0.54 eV, which is still lower than those of pure transition-metal surfaces. Therefore, although the limiting potential is not always determined by the CO -to- CHO step, targeting the CO – CHO scaling, in this case, is a viable strategy to achieve better CO_2 catalysis, in terms of computational screening and catalyst design. The resultant limiting potential for MoS_2 with Ni and Co dopants are both lower than those of pure transition-metal surfaces, leading to an improved catalytic efficiency.

Selectivity between CO_2 Reduction and Hydrogen Evolution. In addition to efficiency, we also evaluated a rough measure of the selectivity between CO_2 reduction and hydrogen evolution reaction (HER) of these materials; the results are shown in Figure 8. The limiting potential of CO , which is denoted as $U_L(\text{CO})$, defines the overall efficiency of CO_2 reduction to more-reduced products beyond CO , thus representing the activity of CO_2 reduction. Similarly, the limiting potential of H_2 , which is denoted as $U_L(\text{H}_2)$, represents the activity of HER. Therefore, the difference between $U_L(\text{CO})$ and $U_L(\text{H}_2)$, $U_L(\text{CO}) - U_L(\text{H}_2)$, suggests the selectivity between CO_2 reduction and HER. While a rigorous analysis of selectivity requires consideration of barriers the resultant kinetics, this limiting potential approach has been shown to be consistent with the trends in selectivity of CO_2 reduction versus HER on transition metals.^{5c} Using this simple analysis, nickel is suggested to be the most selective and reactive among all nonprecious metal dopants. In addition, the stability of Ni-doped sulfur edge of MoS_2 is evaluated through the thermodynamics of vacancy formation via dissociation of COS , and is discussed in the Supporting Information.²¹

How Doped MoS_2 Breaks Linear Scaling among CO_2 Reduction Intermediates. The dual binding sites of the doped MoS_2 create the structural basis for its unorthodox scaling relationship. Unlike pure transition-metal surfaces, these metal/*p*-block materials provide two different binding sites for the CO_2 reduction intermediates: a metallic site (dopant metal) for CO^* and a covalent site (sulfur) for COOH^* and CHO^* , as shown in Figure 9.²² Therefore, during the reduction from CO^* to CHO^* , the reaction intermediate switches from metal sites to S sites, and a significant stabilization of the CHO^* is achieved. This is the key difference between the pure transition-metal surfaces and MoS_2 .

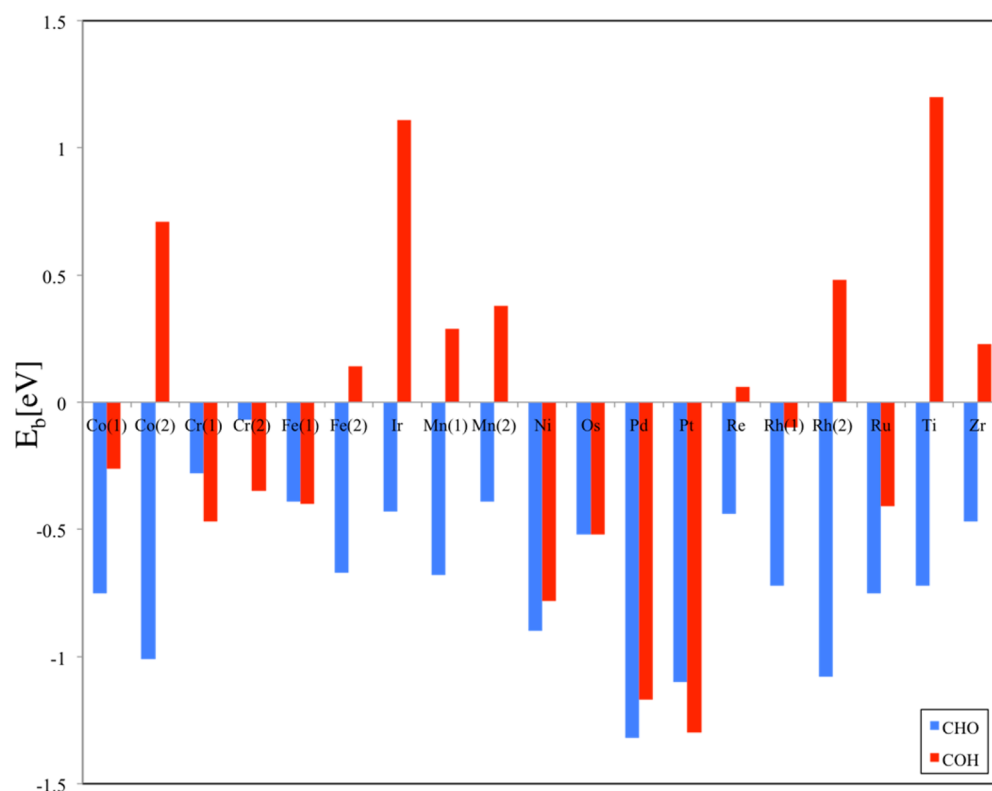


Figure 5. Binding energies $E_b(\text{CHO})$ vs $E_b(\text{COH})$ for the doped sulfur edge of MoS_2 .

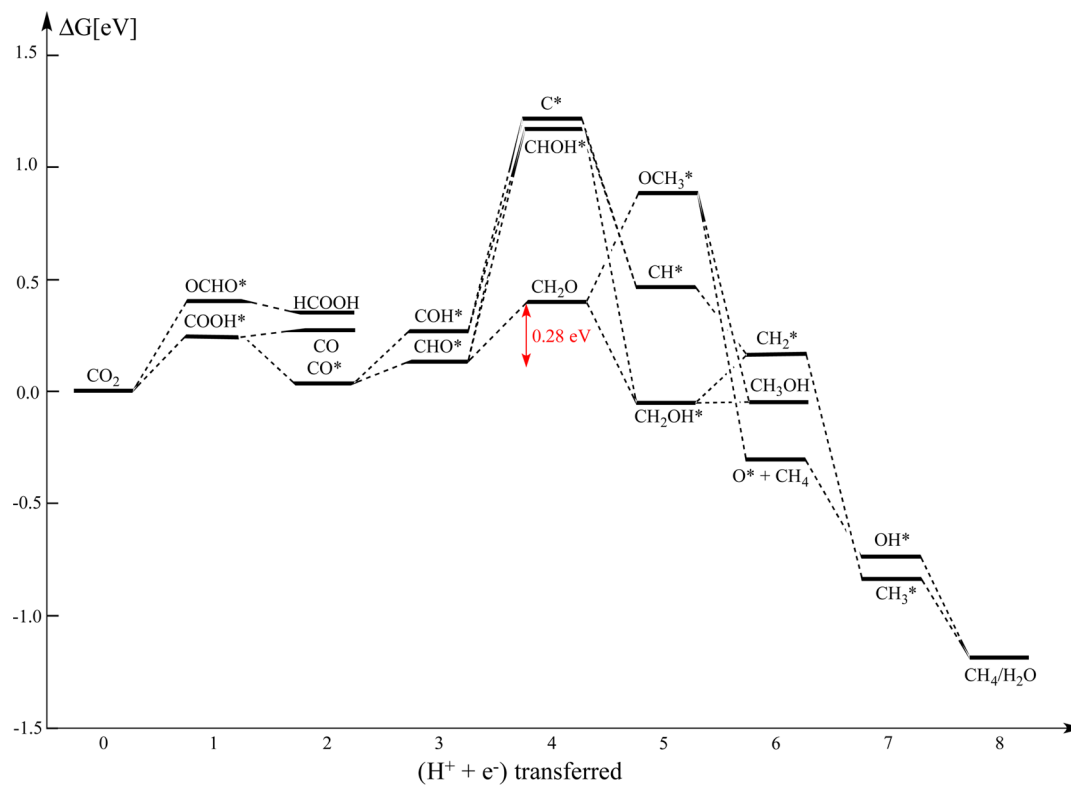


Figure 6. Free-energy changes of CO_2 reduction catalytic cycle on the Ni-doped sulfur edge of MoS_2 at the applied potential of 0 V.

To illustrate the structural basis of the unique scaling, the scaling relationships between intermediates bound to the same site are shown in Figures 10 and 11. All adsorbate configurations have been relaxed to local minima corresponding

to the site considered. In this case, linear scaling relationships do exist. The linear scaling relationships for the metallic site are highlighted in green and is worse for CO_2 activity, relative to the scaling on transition-metal (111) and (211) surfaces. The

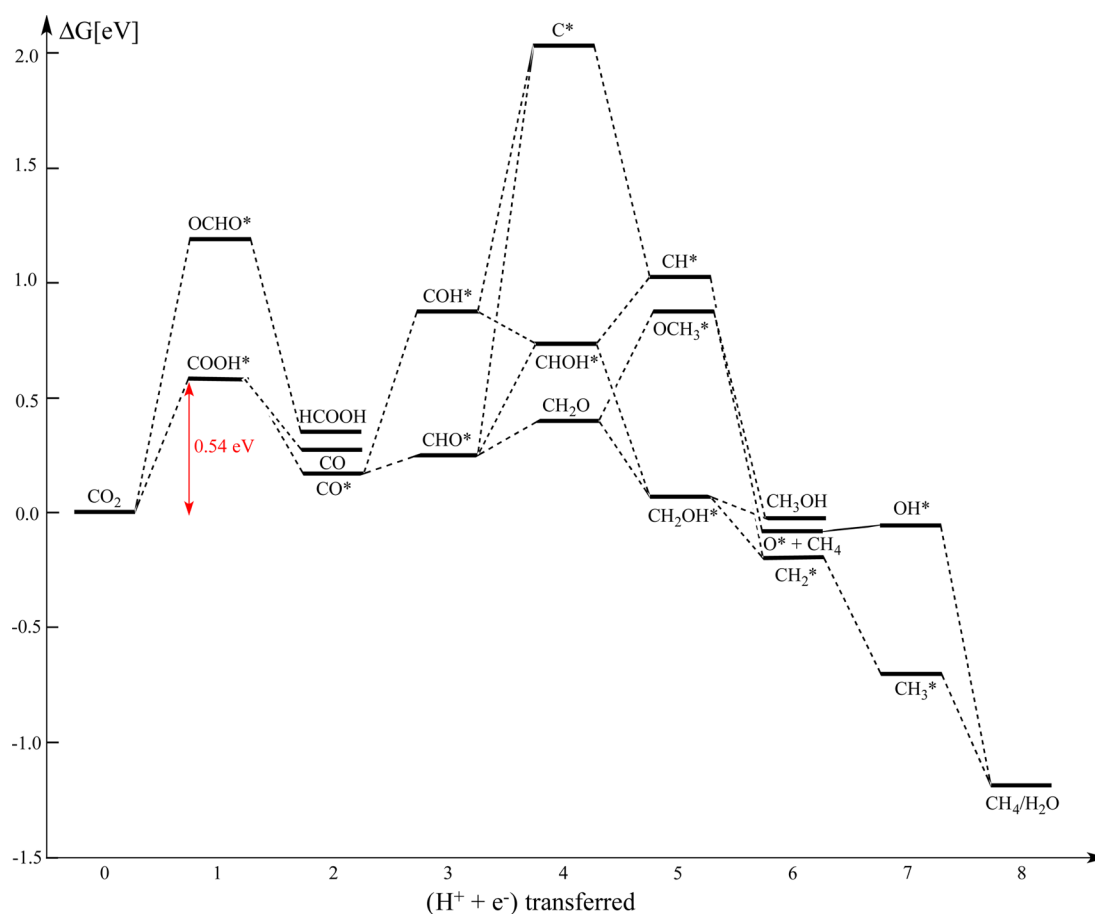


Figure 7. Free-energy changes of CO₂ reduction catalytic cycle on the Co-doped sulfur edge of MoS₂ at the applied potential of 0 V.

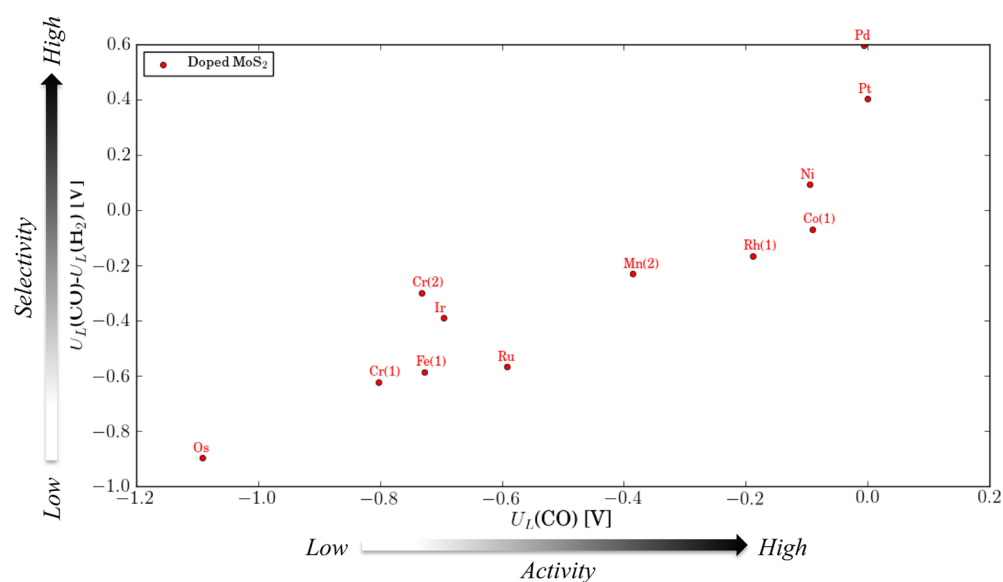


Figure 8. Difference between limiting potentials of CO and H₂ (thermodynamic indicator of selectivity) versus the limiting potential of CO for CO reduction on the variously doped sulfur edge of MoS₂.

linear scaling relationships for the sulfur site are highlighted in red, and shows a much weaker binding energy for CO*, relative to COOH* and CHO*.

Interestingly, the scalings on the metallic and sulfur sites have significantly different slopes. This difference can be rationalized using our previous study on the scaling behavior of transition-

metal surfaces.²³ The available valency of the adsorbate determines the slope of the scaling. Binding to the metallic site is similar to the binding of a transition-metal surface since the major interactions are through the metallic atom, and COOH, CO, and CHO have similar available valency. This suggests that the scaling relationship should have a slope of ~ 1 ,

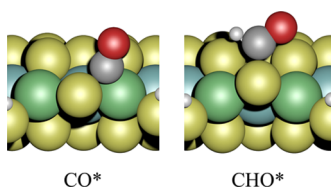


Figure 9. Binding configurations of CO* and CHO* on the Ni-doped sulfur edge of MoS₂. CHO* binds to the bridging S atoms, whereas CO* binds to the Ni atoms.

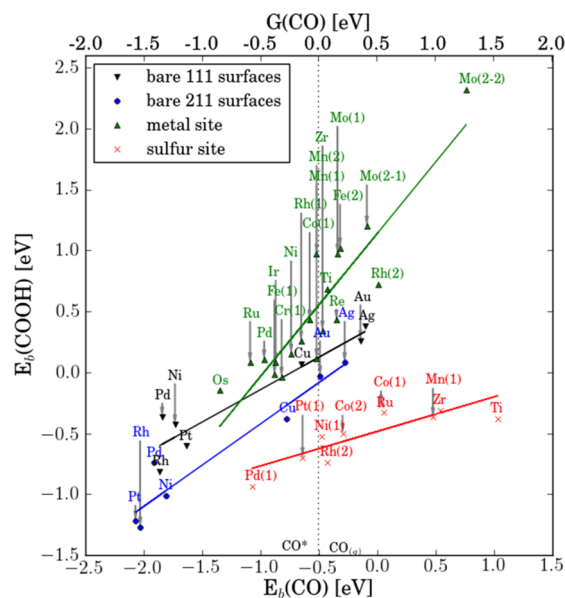


Figure 10. Binding energies $E_b(\text{COOH})$ vs $E_b(\text{CO})$ for the metal and sulfur site of doped sulfur edge of MoS₂, as well as the transition-metal (111) and (211) scaling relations.

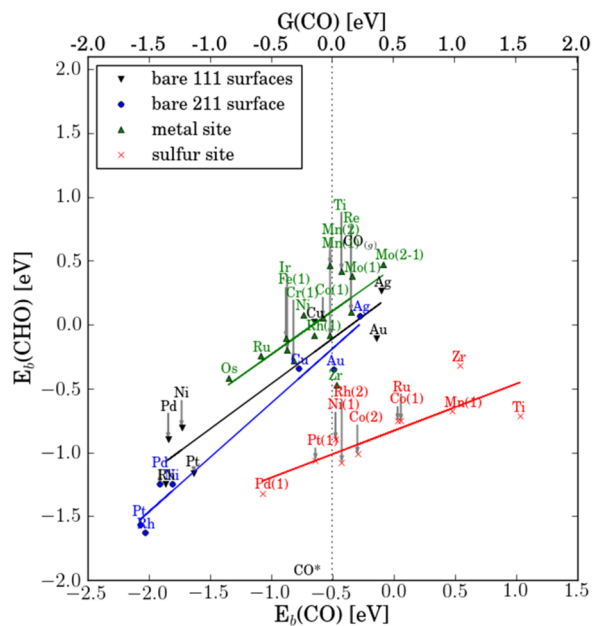


Figure 11. Binding energies $E_b(\text{CHO})$ vs $E_b(\text{CO})$ for the metal and sulfur site of doped sulfur edge of MoS₂, as well as the transition-metal (111) and (211) scaling relations.

which is consistent with the results in Figures 10 and 11; the slope of $E_b(\text{COOH})$ vs $E_b(\text{CO})$ is 1.16 and the slope of

$E_b(\text{CHO})$ vs $E_b(\text{CO})$ is 0.77. When binding to the sulfur site, the slopes of both scaling lines are very small. $E_b(\text{CO})$ does not change significantly vs $E_b(\text{COOH})$ or $E_b(\text{CHO})$ (red lines in Figures 10 and 11). This can also be rationalized in the same way. The adsorption of COOH, CO, CHO on the sulfur site can be considered as adsorption of SCO₂, SCO, SCHO on the dopant metal defect. SCO₂ and SCO both have a valency of 1, while SCHO has a valency of zero. Therefore, the slopes of the $E_b(\text{SCO}_2)$ vs $E_b(\text{SCO})$ and $E_b(\text{SCHO})$ vs $E_b(\text{SCO})$ scaling lines should both be very low. As shown in Figures 10 and 11 (red lines), the slope of $E_b(\text{COOH})$ vs $E_b(\text{CO})$ on a sulfur site has a slope of 0.28, and that for $E_b(\text{CHO})$ vs $E_b(\text{CO})$ is 0.37. Because of these two dramatically slopes, the strongest binding energies for the adsorbates generally shift away from transition-metal scaling and toward the desired region of high efficiency for CO₂ reduction.

Binding Analysis of CO*. To rationalize the weak binding of CO on the sulfur site, a distortion/interaction model²⁴ and electron density analysis are applied to the CO adsorption of the sulfur edge, using Ni-doped MoS₂ as an example. The adsorption of CO on the metallic site is 0.25 eV weaker than the adsorption on sulfur site. As shown in Figures 12 and 13, we separate the CO adsorption energy into four terms:

- (1) The distortion energy of CO, which is denoted as $E_{\text{dist}}(\text{CO})$ and is defined as the energy difference between the ground state of CO and its distorted geometry in the adsorbed slab. $E_{\text{dist}}(\text{CO})$ quantifies the geometric change of CO upon the adsorption.
- (2) The distortion energy of the slab, which is denoted as $E_{\text{dist}}(\text{slab})$ and is defined as the energy difference between the energy of the bare slab and its distorted geometry in the adsorbed slab. $E_{\text{dist}}(\text{slab})$ quantifies the geometric change of the slab upon the adsorption.
- (3) The interaction energy, which is denoted as E_{int} and is defined as the energy difference between the adsorbed slab and the separate distorted fragments (slab and CO). E_{int} describes the strength of the interaction between the distorted CO and the distorted slab.
- (4) The solvation energy correction for the adsorbed CO, which is E_{sol} as determined in previous work.^{5a}

Therefore,

$$E_b(\text{CO}) = E_{\text{dist}}(\text{CO}) + E_{\text{dist}}(\text{slab}) + E_{\text{int}} + E_{\text{sol}}$$

The distortion/interaction analysis shows that the distortion of the slab is the primary contributor to the 0.25 eV difference in binding energy between the sulfur and metallic site. $E_{\text{dist}}(\text{slab}) = 0.99$ eV for CO adsorption on the sulfur site, while it only requires 0.50 eV distortion of the slab for CO to adsorb on the metallic site. Such change in the slab distortion is related to the S–Ni bond of the sulfur edge in the Ni-doped MoS₂. Upon adsorption on the sulfur site, CO forms a “SCO” moiety, which is isoelectronic with CO₂. This closed-shell species binds weakly to the rest of the slab, weakening the existing Ni–S bond of the sulfur edge, and significant energy is required for this distortion. In contrast, CO adsorption on the metallic site creates a “NiCO” moiety, and this open-shell moiety binds the rest of the slab stronger than “SCO”, and less distortion is required for CO adsorption on the metallic site.

A similar distortion/interaction argument can be applied to rationalize the scaling of $E_b(\text{CO})$ vs $E_b(\text{CHO})$ of the sulfur site of doped MoS₂. Compared to the “SCO” moiety of the CO adsorption, the adsorption of *CHO creates a “SCHO” open-

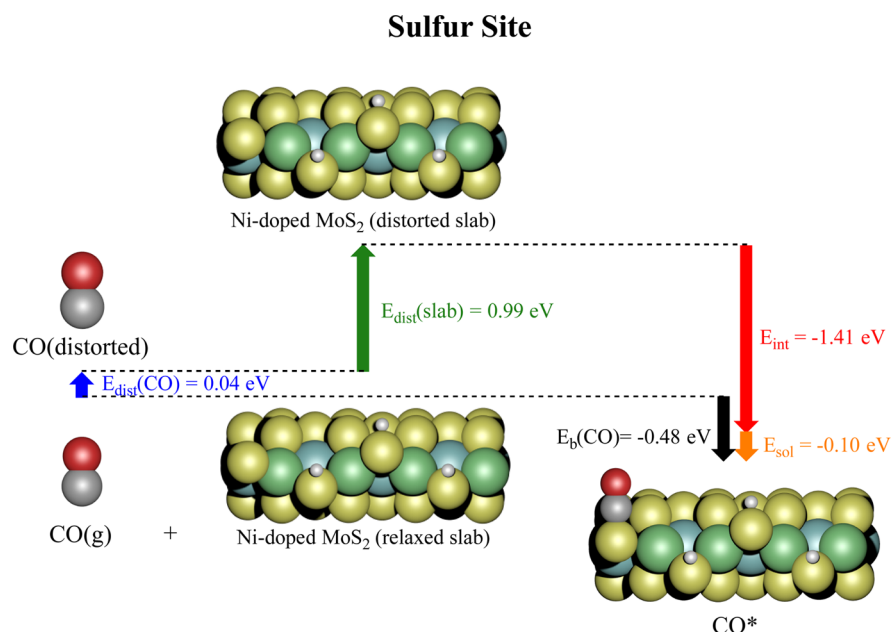


Figure 12. Distortion/interaction analysis of CO adsorption on sulfur site of Ni-doped MoS₂.

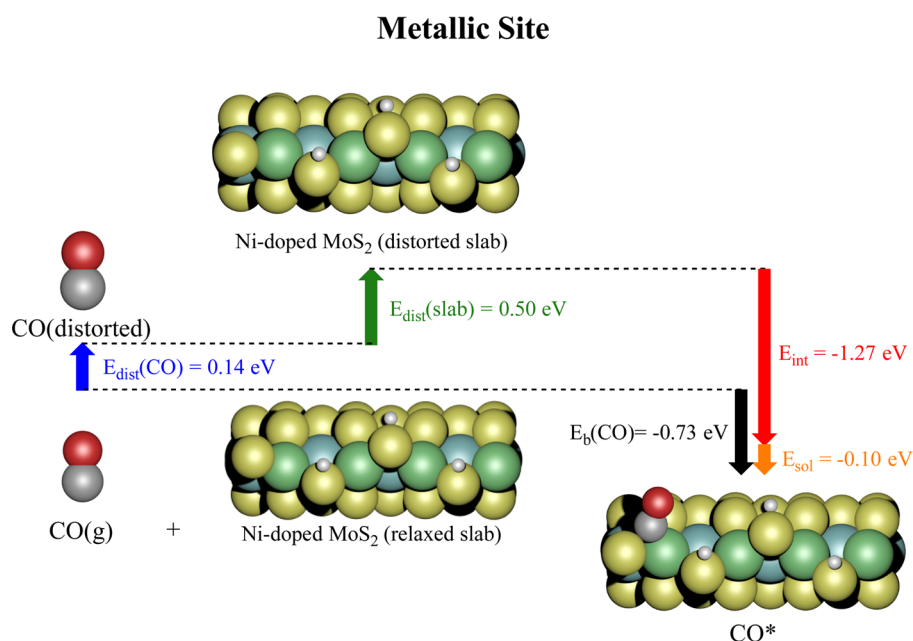


Figure 13. Distortion/interaction analysis of CO adsorption on metallic site of Ni-doped MoS₂.

shell moiety, isoelectronic with *OCHO, and this open-shell species binds stronger to the slab than the closed-shell "SCO" moiety. Indeed, the distortion of slab for the *CHO adsorption on the sulfur site is only 0.27 eV, which is significantly less than the 0.99 eV slab distortion for the corresponding CO adsorption.

To illustrate the change in the strength of the Ni–S bond, we calculate charge density difference isosurfaces calculated using the densities of SCHO* and SCO* as adsorbate references:

$$\Delta\rho = \rho(\text{surf} + \text{ads}) - \rho(\text{ads}) - \rho(\text{surf}) \quad (1)$$

Figure 14 shows that the electron density of the neighboring S–Ni bond increases (blue regions) with the adsorption of *CHO, which is consistent with the postulated strong interaction between the open-shell "SCHO" moiety and the

rest of the slab. In contrast, electron density (red) decreases in the Ni–S region with the adsorption of *CO. This confirms our hypothesis that the closed-shell "SCO" weakens the interaction in the slab, leading to high distortion and low adsorption energy.

The nature of the bonds formed at the S and M site are illustrated using the CO* and CHO* densities as adsorbate references in eq 1, and are shown in Figure 15. When CHO* and CO* bind to the sulfur site, *s*-bond formation to the S is observed. Where CO* binds to the Ni, *s*-donation from the carbon as well as *p*-back bonding to the *p** CO orbital characteristic of CO–metal bonds.

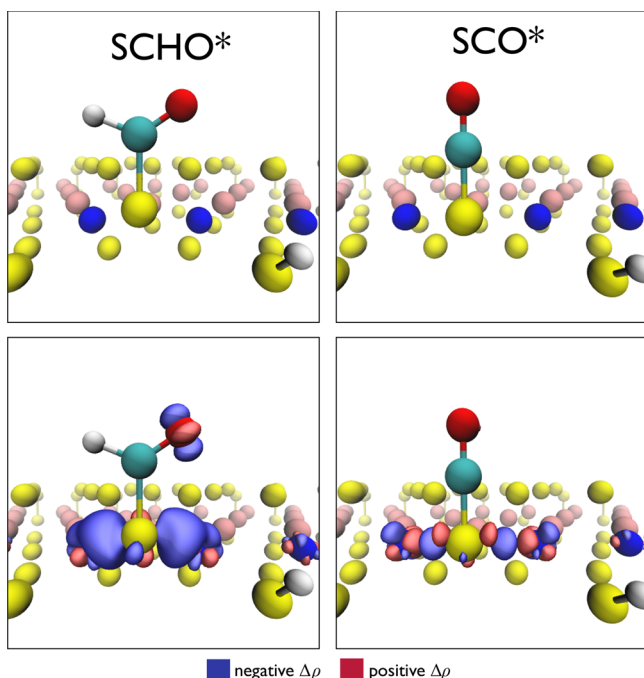


Figure 14. Charge density isosurfaces upon CHO* and CO* adsorption on the sulfur site of Ni-doped MoS₂, using SCHO* and SCO* as references. The purple region represents the negative charge density difference of $-0.008 \text{ e Bohr}^{-1}$, and red region represents the positive charge density difference of $+0.008 \text{ e Bohr}^{-1}$.

CONCLUSIONS

Improved catalytic activity of CO₂ reduction beyond existing transition-metal surfaces requires the breaking of the linear scaling relations between the binding energies of reduction intermediates. We have found doped MoS₂ to show significant

deviations from transition-metal scaling in the direction of improved CO₂ reduction activity. The deviation from transition-metal scaling arises from the metal and sulfur binding sites. These two sites create two different linear scaling relationships: one for the dopant metal and another for sulfur. When the strongest binding site for each adsorbate is considered, the CO* binding energy is significantly weaker than that of COOH* or CHO*. This trend results in an overall deviation from the linear scaling on pure transition-metal surfaces. This principle should apply to other metal/*p*-block materials, where two binding sites are available. Distortion/interaction and electron density analysis showed the origins of the scaling relations on the sulfur site. When CO binds to the sulfur site, it creates a close-shell “SCO” moiety, which weakens the neighboring S–Ni bond and increases the distortion of slab. In contrast, CHO* binding creates an open-shell “SCHO” moiety, and strong neighboring S–Ni interactions can still be maintained, leading to only a small distortion energy. Charge density difference isosurfaces showed the corresponding change of electron density on the slab upon the CO and CHO adsorption. The weakening of the S–Ni bond is associated with decreasing electron density, while CHO adsorption increases the electron density of the neighboring S–Ni region.

Generally, favorable thermochemical reaction energies are a necessary but not sufficient condition for a viable catalyst. Therefore, the determination of kinetic proton–electron transfer barriers and selectivities is critical for future catalyst design. These are subjects of ongoing research in our laboratory.

ASSOCIATED CONTENT

Supporting Information

The Supporting Information is available free of charge on the ACS Publications website at DOI: 10.1021/acscatal.6b00619.

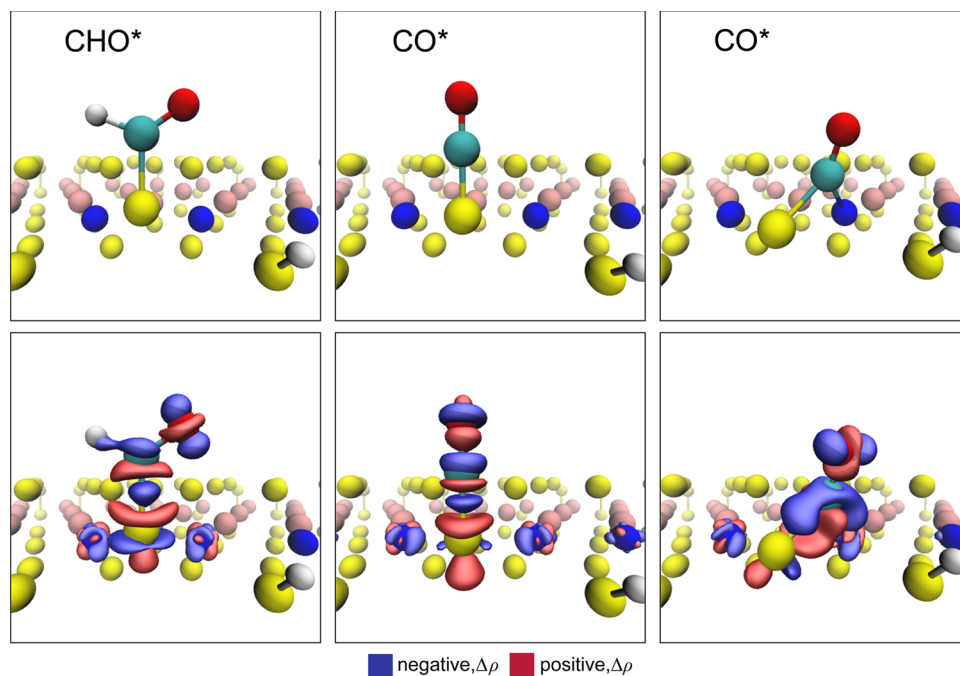


Figure 15. Charge density isosurfaces upon CHO* and CO* adsorption on the sulfur site of Ni-doped MoS₂, using CHO* and CO* as references. The purple region represents the negative charge density difference of $-0.005 \text{ e Bohr}^{-1}$, and red region represents the positive charge density difference of $+0.005 \text{ e Bohr}^{-1}$.

Further details of DFT calculations and coverage determination; details of computational hydrogen electrode and example; stability evaluation of Ni-doped sulfur edge of MoS₂ through COS dissociation ([PDF](#))

AUTHOR INFORMATION

Corresponding Author

*E-mail: norskjov@stanford.edu.

Author Contributions

The manuscript was written through contributions of all authors. All authors have given approval to the final version of the manuscript.

Author Contributions

[§](X.H., K.C.) These authors contributed equally.

Notes

The authors declare no competing financial interest.

ACKNOWLEDGMENTS

We acknowledge support from the Global Climate Energy Project (GCEP) at Stanford University (Fund No. 52454). This material is based upon work performed by the Joint Center for Artificial Photosynthesis, a DOE Energy Innovation Hub, supported through the Office of Science of the U.S. Department of Energy (under Award No. DE-SC0004993). This research used resources of the National Energy Research Scientific Computing Center, a DOE Office of Science User Facility supported by the Office of Science of the U.S. Department of Energy, under Contract No. DE-AC02-05CH11231.

REFERENCES

- (1) (a) Gattrell, M.; Gupta, N.; Co, A. *J. Electroanal. Chem.* **2006**, *594*, 1–19. (b) Kuhl, K. P.; Cave, E. R.; Abram, D. N.; Jaramillo, T. F. *Energy Environ. Sci.* **2012**, *5*, 7050–7059.
- (2) For reviews, see: (a) Benson, E. E.; Kubiak, C. P.; Sathrum, A. J.; Smieja, J. M. *Chem. Soc. Rev.* **2009**, *38*, 89–99. (b) Rakowski Dubois, M.; Dubois, D. L. *Acc. Chem. Res.* **2009**, *42*, 1974–1982. (c) Qiao, J.; Liu, Y.; Hong, F.; Zhang, J. *Chem. Soc. Rev.* **2014**, *43*, 631–675. For recent works on kinetic barriers of CO₂ reduction, see: (d) Nie, X.; Esopi, M. R.; Janik, M. J.; Asthagiri, A. *Angew. Chem., Int. Ed.* **2013**, *52*, 2459–2462. (e) Luo, W.; Nie, X.; Janik, M. J.; Asthagiri, A. *ACS Catal.* **2016**, *6*, 219–229.
- (3) Li, C. W.; Kanan, M. W. *J. Am. Chem. Soc.* **2012**, *134*, 7231–7234.
- (4) (a) Hori, Y.; Murata, A.; Kikuchi, K.; Suzuki, S. *J. Chem. Soc., Chem. Commun.* **1987**, 728–729. (b) Hori, Y. *Modern Aspects of Electrochemistry*, Vol. 42; Vayenas, C. G., White, R. E., Gamboa-Aldeco, M. E., Eds.; Springer: New York, 2008; pp 89–189. (c) Chen, Y.; Li, C. W.; Kanan, M. W. *J. Am. Chem. Soc.* **2012**, *134*, 19969–19972.
- (5) (a) Peterson, A. A.; Abild-Pedersen, F.; Studt, F.; Rossmeisl, J.; Nørskov, J. K. *Energy Environ. Sci.* **2010**, *3*, 1311–1315. (b) Peterson, A. A.; Nørskov, J. K. *J. Phys. Chem. Lett.* **2012**, *3*, 251–258. (c) Shi, C.; Hansen, H. A.; Lausche, A. C.; Nørskov, J. K. *Phys. Chem. Chem. Phys.* **2014**, *16*, 4720–4727.
- (6) (a) Hansen, H. A.; Varley, J. B.; Peterson, A. A.; Nørskov, J. K. *J. Phys. Chem. Lett.* **2013**, *4*, 388–392. (b) Kuhl, K. P.; Hatsukade, T.; Cave, E. R.; Abram, D. N.; Kibsgaard, J.; Jaramillo, T. F. *J. Am. Chem. Soc.* **2014**, *136*, 14107–14113. For related studies on breaking scalings, see: (c) Li, H.; Li, Y.; Koper, M. T. M.; Calle-Vallejo, F. J. *J. Am. Chem. Soc.* **2014**, *136*, 15694–15701. (d) Michalsky, R.; Zhang, Y.-J.; Peterson, A. A. *ACS Catal.* **2014**, *4*, 1274–1278. (e) Klaus, S.; Cai, Y.; Louie, M. W.; Trotochaud, L.; Bell, A. T. *J. Phys. Chem. C* **2015**, *119*, 7243–7254. (f) Swierk, J.; Klaus, S.; Trotochaud, L.; Bell, A. T.; Tilley, T. D. *J. Phys. Chem. C* **2015**, *119*, 19022–19029.
- (7) (a) Tsai, C.; Chan, K.; Nørskov, J. K.; Abild-Pedersen, F. *J. Phys. Chem. Lett.* **2014**, *5*, 3884–3889. (b) Tsai, C.; Chan, K.; Abild-Pedersen, F.; Nørskov, J. K. *Phys. Chem. Chem. Phys.* **2014**, *16*, 13156–13164. (c) Chan, K.; Tsai, C.; Hansen, H. A.; Nørskov, J. K. *ChemCatChem* **2014**, *6*, 1899–1905. (d) Tsai, C.; Abild-Pedersen, F.; Nørskov, J. K. *Nano Lett.* **2014**, *14*, 1381–1387. (e) Tsai, C.; Chan, K.; Nørskov, J. K.; Abild-Pedersen, F. *Catal. Sci. Technol.* **2015**, *5*, 246–253.
- (8) (a) Asadi, M.; Kumar, B.; Behranginia, A.; Rosen, B. A.; Baskin, A.; Repnin, N.; Pisasale, D.; Phillips, P.; Zhu, W.; Haasch, R.; Klie, R. F.; Kral, P.; Abiade, J.; Salehi-Khojin, A. *Nat. Commun.* **2014**, *5*, 4470. For related homogeneous reduction of CO₂ with Mo catalysts, see: (b) Clark, M. L.; Grice, K. A.; Moore, C. E.; Rheingold, A. L.; Kubiak, C. P. *Chem. Sci.* **2014**, *5*, 1894–1900. (c) Sieh, D.; Lacy, D. C.; Peters, J. C.; Kubiak, C. P. *Chem.—Eur. J.* **2015**, *21*, 8497–8503.
- (9) For related studies using the same model, see: (a) Hinnemann, B.; Moses, P. G.; Bonde, J.; Jørgensen, K. P.; Nielsen, J. H.; Hørch, S.; Chorkendorff, I.; Nørskov, J. K. *J. Am. Chem. Soc.* **2005**, *127*, 5308–5309. (b) Bollinger, M.; Jacobsen, K. W.; Nørskov, J. K. *Phys. Rev. B: Condens. Matter Mater. Phys.* **2003**, *67*, 085410.
- (10) (a) Helveg, S.; Lauritsen, J.; Lægsgaard, E.; Stensgaard, I.; Nørskov, J. K.; Clausen, B. S.; Topsøe, H.; Besenbacher, F. *Phys. Rev. Lett.* **2000**, *84*, 951–954. (b) Byskov, L. S.; Nørskov, J. K.; Clausen, B. S.; Topsøe, H. *Catal. Lett.* **2000**, *64*, 95–99. (c) Lauritsen, J. V.; Bollinger, M. V.; Lægsgaard, E.; Jacobsen, K. W.; Nørskov, J. K.; Clausen, B. S.; Topsøe, H.; Besenbacher, F. *J. Catal.* **2004**, *221*, 510–522. For a related study on electrocatalysis of Ni-Mo, see: (d) Shaner, M. R.; McKone, J. R.; Gray, H. B.; Lewis, N. S. *Energy Environ. Sci.* **2015**, *8*, 2977–2984.
- (11) (a) Schweiger, H.; Raybaud, P.; Kresse, G.; Toulhoat, H. *J. Catal.* **2002**, *207*, 76–87. (b) Schweiger, H.; Raybaud, P.; Toulhoat, H. *J. Catal.* **2002**, *212*, 33–38.
- (12) Giannozzi, P.; Baroni, S.; Bonini, N.; Calandra, M.; Car, R.; Cavazzoni, C.; Chiarotti, C.; Ceresoli, D.; Chiarotti, G. L.; Cococcioni, M.; Dabo, I.; et al. *J. Phys.: Condens. Matter* **2009**, *21*, 395502.
- (13) (a) Wellendorff, J.; Lundgaard, K. T.; Møgelhøj, A.; Petzold, V.; Landis, D. D.; Nørskov, J. K.; Bligaard, T.; Jacobsen, K. W. *Phys. Rev. B: Condens. Matter Mater. Phys.* **2012**, *85*, 235149. (b) Dion, M.; Rydberg, H.; Schroder, E.; Langreth, D. C.; Lundqvist, B. I. *Phys. Rev. Lett.* **2004**, *92*, 246401. (c) Thonhauser, T.; Cooper, V. R.; Li, S.; Puzder, A.; Hyldgaard, P.; Langreth, D. C. *Phys. Rev. B: Condens. Matter Mater. Phys.* **2007**, *76*, 125112.
- (14) Young, P. J. *Phys. D: Appl. Phys.* **1968**, *1*, 936–938.
- (15) Nørskov, J. K.; Rossmeisl, J.; Logadottir, A.; Lindqvist, L.; Kitchin, J. R.; Bligaard, T.; Jonsson, H. *J. Phys. Chem. B* **2004**, *108*, 17886–17892.
- (16) (a) Rossmeisl, J.; Chan, K.; Ahmed, R.; Tripković, V.; Björketun, M. E. *Phys. Chem. Chem. Phys.* **2013**, *15*, 10321–10325. (b) Chan, K.; Eikerling, M. *Phys. Chem. Chem. Phys.* **2014**, *16*, 2106–2117. (c) Montoya, J.; Shi, C.; Chan, K.; Nørskov, J. K. *J. Phys. Chem. Lett.* **2015**, *6*, 2032–2037. (d) Rossmeisl, J.; Chan, K.; Skúlason, E.; Björketun, M. E.; Tripković, V. *Catal. Today* **2016**, *262*, 36–40.
- (17) Shi, C.; O'Grady, C. P.; Peterson, A. A.; Hansen, H. A.; Nørskov, J. K. *Phys. Chem. Chem. Phys.* **2013**, *15*, 7114–7122.
- (18) Bligaard, T.; Nørskov, J. K.; Dahl, S.; Matthiesen, J.; Christensen, C. H.; Sehested, J. *J. Catal.* **2004**, *224*, 206–217.
- (19) Plessow, P. N.; Abild-Pedersen, F. *J. Phys. Chem. C* **2015**, *119*, 10448–10453.
- (20) Nørskov, J. K.; Bligaard, T.; Logadottir, A.; Kitchin, J.; Chen, J.; Pandelov, S.; Stimming, U. *J. Electrochem. Soc.* **2005**, *152*, J23–J26.
- (21) The stability of the Ni-doped sulfur edge is studied through the thermodynamics of COS dissociation. Further details are included in the [Supporting Information](#).
- (22) For related studies on electrocatalysis with metal/*p*-block materials, see: (a) Mi, Q. X.; Coridan, R. H.; Brunschwig, B. S.; Gray, H. B.; Lewis, N. S. *Energy Environ. Sci.* **2013**, *6*, 2646–2653. (b) Mi, Q. X.; Zhanaidarova, A.; Brunschwig, B. S.; Gray, H. B.; Lewis, N. S. *Energy Environ. Sci.* **2012**, *5*, 5694–5700. (c) Lichterman, M. F.; Carim, A. I.; McDowell, M. T.; Hu, S.; Gray, H. B.; Brunschwig, B. S.; Lewis, N. S. *Energy Environ. Sci.* **2014**, *7*, 3334–3337. (d) Saadi, F. H.; Carim, A. I.; Velazquez, J. M.; Baricuatro, J. H.; McCrory, C. C. L.

Soriaga, M. P.; Lewis, N. S. *ACS Catal.* **2014**, *4*, 2866–2873. (e) Carim, A. I.; Saadi, F. H.; Soriaga, M. P.; Lewis, N. S. *J. Mater. Chem. A* **2014**, *2*, 13835–13839. (f) Velazquez, J. M.; Saadi, F. H.; Pieterick, A. P.; Spurgeon, J. M.; Soriaga, M. P.; Brunschwig, B. S.; Lewis, N. S. *J. Electroanal. Chem.* **2014**, *716*, 45–48. (g) Hu, S.; Shaner, M. R.; Beardslee, J. A.; Lichterman, M.; Brunschwig, B. S.; Lewis, N. S. *Science* **2014**, *344*, 1005–1009.

(23) Abild-Pedersen, F.; Greeley, J.; Studt, F.; Rossmeisl, J.; Munter, T. R.; Moses, P. G.; Skúlason, E.; Bligaard, T.; Nørskov, J. K. *Phys. Rev. Lett.* **2007**, *99*, 016105.

(24) For selected publications on distortion/interaction model, see:

(a) Ess, D. H.; Houk, K. N. *J. Am. Chem. Soc.* **2007**, *129*, 10646–10647. (b) Legault, C. Y.; Garcia, Y.; Merlic, G. A.; Houk, K. N. *J. Am. Chem. Soc.* **2007**, *129*, 12664–12665. (c) Ess, D. H.; Houk, K. N. *J. Am. Chem. Soc.* **2008**, *130*, 10187–10198. (d) van Zeist, W.-J.; Bickelhaupt, F. M. *Org. Biomol. Chem.* **2010**, *8*, 3118–3127. (e) Usharani, D.; Lacy, D. C.; Borovik, A. S.; Shaik, S. *J. Am. Chem. Soc.* **2013**, *135*, 17090–17104. (f) Yang, Y.-F.; Cheng, G.-J.; Liu, P.; Leow, D.; Sun, T.-Y.; Chen, P.; Zhang, X.; Yu, J.-Q.; Wu, Y.-D.; Houk, K. N. *J. Am. Chem. Soc.* **2014**, *136*, 344–355. (g) Hong, X.; Liang, Y.; Houk, K. N. *J. Am. Chem. Soc.* **2014**, *136*, 2017–2025.